Bottom stress generation and sediment transport over the shelf and slope off of Lake Superior's Keweenaw peninsula

James H. Churchill and Albert J. Williams
Woods Hole Oceanographic Institution, Woods Hole, Massachusetts, USA

Elise A. Ralph
Large Lakes Observatory, University of Minnesota at Duluth, Duluth, Minnesota, USA

Received 6 June 2003; revised 26 May 2004; accepted 27 August 2004; published 30 October 2004.

[1] Data from near-bottom instruments reveal that the mechanisms responsible for generating bottom stresses and resuspending sediment over the shelf and slope off of Lake Superior's Keweenaw peninsula exhibit distinct seasonal variations. Notably, near-bottom flows over the slope are persistently weak (<10 cm s^{-1}) during summer but frequently attain high speeds, in excess of 20 cm s^{-1}, in autumn and winter. During the intense storms of autumn and winter the generation of bottom stress is enhanced by the action of near-bottom orbital velocities due to surface waves. Even at 90-m depth, orbital velocities can increase bottom stress by a factor of up to 20% during storms. Where the seasonal thermocline intersects the lake floor, bottom stress is also considerably enhanced, often by more than a factor of 2, by high-frequency motions in the internal wave band. Over the Keweenaw slope, sediment resuspension is largely confined to autumn and winter episodes of high bottom stress. Our analysis indicates that this resuspended material tends to be carried offshore, a phenomenon that is partly due to the coincidence of the direction of the buoyancy-driven component of the Keweenaw Current with downwelling favorable alongshore winds. As a result of this coincidence, currents and bottom stresses tend to be greater during periods of downwelling, as opposed to upwelling, circulation. A potential challenge to modeling storm-driven resuspension in the study region is indicated by observations that the minimum stress required for resuspension may vary significantly with time over the autumn and winter. *INDEX TERMS:* 4558 Oceanography: Physical: Sediment transport; 4211 Oceanography: General: Benthic boundary layers; 4239 Oceanography: General: Limnology; *KEYWORDS:* sediment transport, sediment dynamics, bottom boundary layer dynamics

Citation: Churchill, J. H., A. J. Williams, and E. A. Ralph (2004), Bottom stress generation and sediment transport over the shelf and slope off of Lake Superior's Keweenaw peninsula, *J. Geophys. Res.*, *109*, C10S04, doi:10.1029/2003JC001997.

1. Introduction

[2] Because fine particles in nearshore waters typically carry a significant load of substances deemed to be of ecological importance, such as particulate contaminants and organic carbon, the cross-margin transport of fine-grained solids has long been considered a phenomenon worthy of scientific scrutiny. Over the past few decades, studies within the coastal environment have significantly advanced the understanding of processes effecting the resuspension and transport of fine sediment in nearshore waters. These processes include the interaction of storm-driven flows and currents due to surface waves [e.g., *Kang et al.*, 1982; *Lyne et al.*, 1990a; *Sherwood et al.*, 1994; *Wiberg et al.*, 1994], internal wave breaking over steep bathymetry [*Cacchione and Southard*, 1974; *Cacchione and Drake*, 1986], and currents associated with boundary flows or eddies separated from such flows [*Butman*, 1987].

0148-0227/04/2003JC001997$09.00

[3] For a number of reasons, the effects of such processes in large lakes may differ from their effects in the coastal ocean. These include: the smaller fetch in lakes, which tends to limit wave height, and the absence of tides, a principal source of internal wave energy in many oceanic regions. Compared with oceanic examinations of sediment transport, studies of sediment dynamics in large lakes are relatively few; and a large proportion of these have focused on Lake Michigan [e.g., *Liu et al.*, 1984; *Hawley and Lesht*, 1995; *Hawley et al.*, 1996; *Lee and Hawley*, 1998; *Hawley and Lee*, 1999; *Lou et al.*, 2000; *Schwab et al.*, 2000]. Reported measurements pertaining to sediment resuspension in the largest of the Laurentian Great Lakes, Lake Superior, are meager. A notable study, conducted by *Hawley* [2000], involved deployment of an instrumented bottom tripod near the tip of Lake Superior's Keweenaw Peninsula. However, many questions remain regarding sediment dynamics in Lake Superior and water bodies of similar size. These include the impacts of internal wave and surface gravity wave currents on bottom stress generation.

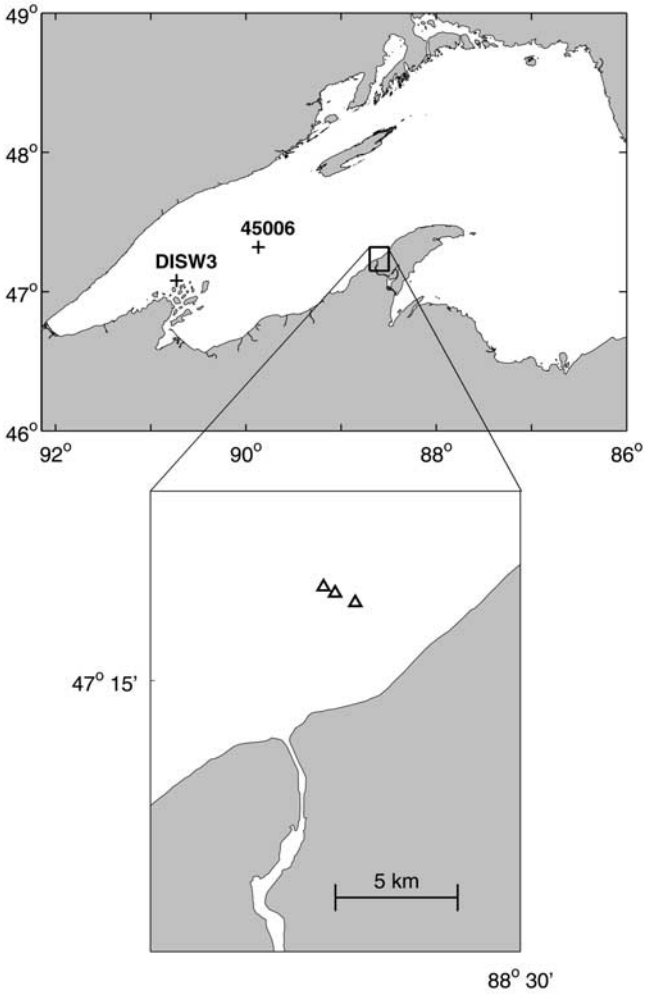

Figure 1. The locations of (top) meteorological stations (crosses) and (bottom) bottom tripods (triangles) from which data used in this study were acquired.

[4] Here we examine these questions, and other issues, using data from instruments moored near the bottom in an area of Lake Superior that is impacted by a seasonal coastal current. A focus of our study, with relevance to other regions impacted by a coastal current, is how the combination of this coastal current and storm-driven flows effects the cross-margin transport of fine material. In the sections to come, we document the seasonal cycles of near-bottom temperature, water velocity and bottom stress in the study region (sections 4.1 and 4.3) and examine conditions under which sediment is resuspended and carried offshore (section 4.4). Also examined is the bottom roughness of the study region (section 4.2). We first describe the study region (section 2) and our analysis procedures (section 3).

2. Setting

[5] Our study is part of the Keweenaw Interdisciplinary Transport Experiment in Superior (KITES). A primary focus of KITES is a seasonal coastal flow known as the Keweenaw Current. Flowing northeastward along the western shoreline of Lake Superior's Keweenaw Peninsula (Figure 1), this current tends to intensify downstream and can reach speeds on the order of 1 m s^{-1} near the tip of the peninsula [*Yeske and Green*, 1975; *Niebauer et al.*, 1977; *Green and Terrell*, 1978; H. J. Niebauer and E. A. Ralph, Episodic events in the Keweenaw Current in Lake Superior: A retrospective, submitted to *Journal of Geophysical Research*, 2004, hereinafter referred to as Niebauer and Ralph, submitted manuscript, 2004]. A numerical modeling investigation by *Chen et al.* [2001] and *Zhu et al.* [2001] has indicated that the Keweenaw Current is partly a thermally driven flow, caused by rapid warming of nearshore (versus offshore) water. As revealed by analysis of moored current meter data by *Niebauer et al.* [1977] and Niebauer and Ralph (submitted manuscript, 2004), the speed of the Keweenaw Current is greatly modulated by fluctuations in the alongshore wind stress due to the passage of high- and low-pressure systems. The current is accelerated by winds directed to the northeast (downwelling favorable) and decelerated by southwestward winds (upwelling favorable). *Niebauer et al.* [1977] have noted that this gives the Keweenaw Current the appearance of a pulsating jet with a period of 4–6 days and an amplitude, near the tip of the peninsula, of roughly 60 cm s^{-1}.

[6] Our study was carried out to the west of the central portions of the Keweenaw Peninsula (Figure 1). On the basis of bottom inclination, the seafloor of this region may be divided into two zones (Figure 2). One is a gently sloping shelf, with a bottom incline of ~0.0045, that extends ~5 km from shore and to roughly the 22-m isobath. The other is an adjacent, steeply inclined slope with an inclination of ~0.06. The sediment grain size distributions over the shelf and slope differ significantly. Analysis of samples from our study region show predominantly coarse surficial sediment over the shelf, with <1% content of silt plus clay (particle diameter <62 μm) and much finer surficial sediment over the slope, with a

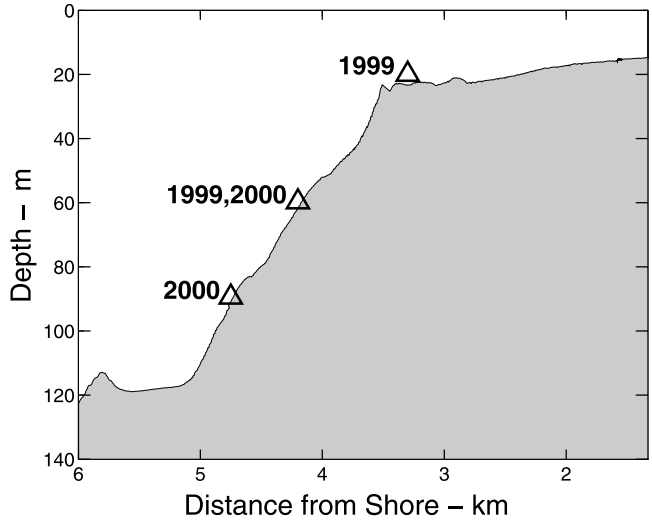

Figure 2. Tripod locations superimposed on a profile of bottom depth along a line nearly passing through the tripod locations. The numbers show the years during which a tripod pair was deployed at the given location.

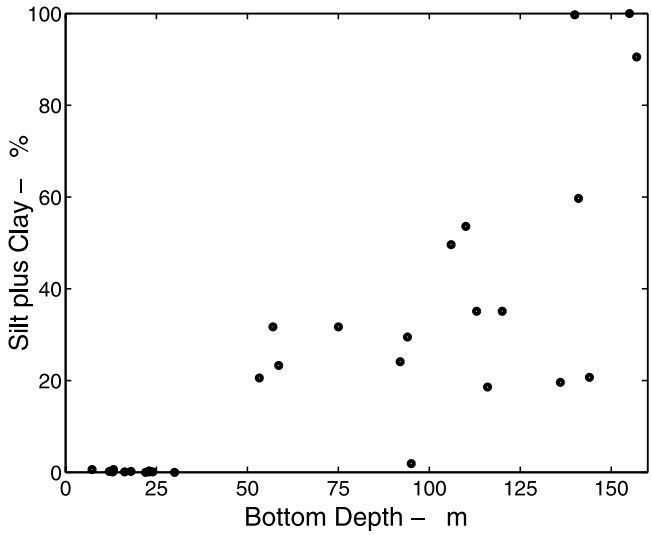

Figure 3. Percentages of silt plus clay (particle diameter <62 μm) in surficial sediment determined from samples acquired along lines that extended across shore and passed within 6 km of the tripod locations.

silt plus clay content of order 30% in the 40–100-m isobath band (Figure 3).

3. Methods

3.1. Field Program

[7] The bulk of the time series data employed in this study came from instruments affixed to two tripods, each of ~5-m height, set on the lake floor. Each tripod supported a Benthic Acoustic Stress Sensor (BASS) array [*Williams et al.*, 1987], consisting of five pulsed acoustic travel time current meters and a pressure sensor (Paroscientific Digiquartz). The BASS current meters were mounted along the tripods' central axes. Each was composed of four transducer pairs that measured velocities (from acoustic travel time differences) within a 12-cm diameter by 12-cm length volume. Mean current meter heights were 0.4, 0.7, 1.3, 2.7, and 4.5 m on one tripod and 0.3, 0.7, 1.3, 2.6, and 4.5 m on the other. Also affixed to each tripod were two temperature sensors and four light back-scattering sensors (LBSSs; WET Labs Inc.). Equipped with a light source and light detector, each LBSS gave a voltage proportional to backscattered light intensity. This voltage was in turn related, through calibration (see below), to suspended particulate mass (SPM) concentration. Two models of LBSS were employed, differing only in sensitivity to SPM. To facilitate computation of SPM flux, each LBSS was set at the same level as a current meter. Sampling from all sensors was done in burst mode. Burst sampling was initiated every 20 min and entailed acquisition of measurements at 2 Hz over a period of 8.5 min.

[8] Deployed near each BASS tripod was a second smaller tripod supporting an in situ particle sampler: the McLane Research Laboratories' Water Transfer System (WTS). These samplers were programmed to acquire a SPM sample once every three days by filtering lake water through a preweighed polycarbonate membrane filter of 47-mm diameter with a 0.4-μm pore size. Each WTS accommodated 24 filters. To acquire samples, the WTSs were programmed to filter a specified maximum volume, either 4 or 5 L, of lake water. This limit was often not achieved, however, because of a programmed featured which halted pumping at or below a specified flow rate. Throughout each pumping cycle, data were collected, at 1 Hz, from a LBSS mounted within 1 cm of the end of the pump intake hose.

[9] The tripods were deployed at sites over the slope and outer shelf west of the central Keweenaw Peninsula (Figures 1 and 2) during two field seasons: 1999 and 2000–2001. Because of a number of factors, including limited battery life and data storage capacity, the tripods needed to be serviced after roughly 60 days of data collection. This divided each field season into a number of separate deployments. Deployment locations and periods differed for each field season. In 1999, tripods were set out in three deployments spanning the time from mid-April through mid-October. In the first two deployments, tripods were set out at the 22- and 60-m isobaths; whereas in the third deployment a single set of tripods was placed at the 60-m isobath. In second field year, the tripods were set out at the 60- and 90-m isobaths over two deployments extending from early August 2000 through mid-January 2001.

[10] The wind data used in our study came from two locations (Figure 1). Wind data used in the analysis of 1999 measurements were from NOAA buoy 45006, located ~100 km to the east of the study region. Because measurements of the 2000–2001 field year extended beyond the yearly removal of buoy 45006, the wind data used in the analysis of these measurements were from the Devils Island C-MAN station, located ~150 km to the east of the study region (labeled DISW3 in Figure 1).

[11] We cannot fully judge the extent to which the winds from these locations are representative of winds at our study site. However, our analysis of data acquired at buoys and C-MAN stations indicate that winds over Lake Superior are highly correlated over 100-km distances. For example, 1999 alongshore wind speeds (along the orientation of the middle Keweenaw) from buoy 45006 and the Devil's Island C-MAN station were correlated at $R^2 = 0.89$. A more extensive analysis of the wind's spatial scale of correlation was undertaken by *Chen et al.* [2004]. They found that the 95% confidence level cutoff of coherence scale over the lake is 350 km for the east-west component of the wind and 280 km for the wind's the south-north component.

[12] All BASS tripod time series data that are presented here have been burst averaged, giving means over each 8.5-min sampling interval. The velocity data shown in some figures have also been low-pass filtered with a 33-hour half-power point filter designed to nearly eliminate fluctuations with periods of less than 20 hours. Velocities have also been rotated into a local coordinate system, with the alongshore axis oriented to coincide with the least squares regression line fit to all the velocity data. In the convention used here, the positive alongshore axis is directed to the northeast and the positive offshore axis is directed offshore to the northwest.

3.2. LBSS Calibration

[13] A primary purpose of the WTS deployment was to acquire in situ data for calibration of the LBSSs; i.e., to

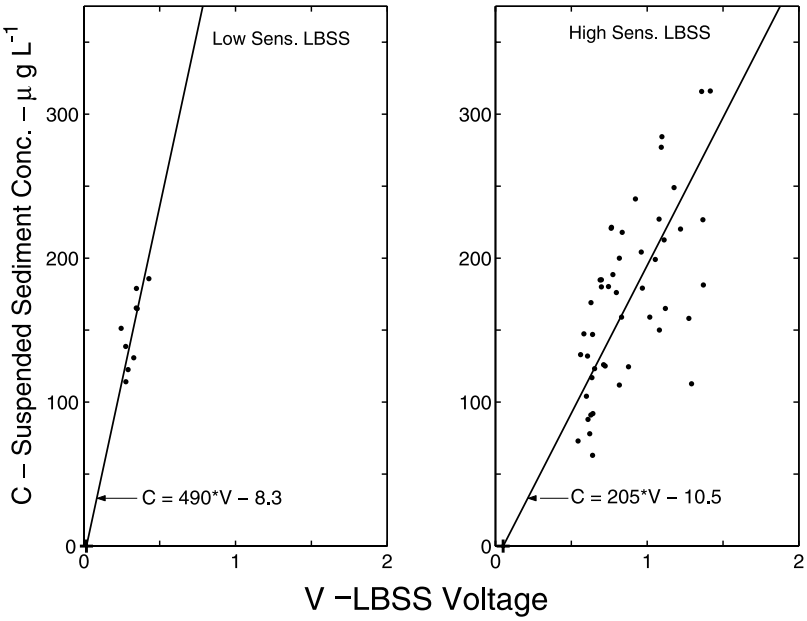

Figure 4. SPM concentration against LBSS voltage for the low- and high-sensitivity LBSS models. The dots are from the WTS samples, and the crosses are from LBSS measurements in water free of SPM. The regression lines were determined by least squares linear regression with the condition that they pass through the zero-SPM points.

derive a formula relating LBSS voltage to SPM concentration. This was deemed necessary because the LBSS response is sensitive to particle size and should critically depend on the local particle size distribution.

[14] Calibration of LBSS voltage also involved acquiring data from LBSSs immersed in particle free water. This was done in the 3-m diameter by 15-m deep calibration tank at the McLane Research Laboratories in Falmouth MA. Data were acquired from each LBSS while immersed in this tank for at least 5 min. The average of all the data from the LBSSs of a particular sensitivity was taken as their representative voltage at zero SPM. The results gave an estimated particle free voltage of 0.017 for the low-sensitivity model and of 0.051 for the high-sensitivity model. The statistical 95% confidence intervals of these values are 0.0014 and 0.0024 volts, respectively.

[15] For each LBSS model sensitivity, a linear calibration curve was determined by fitting a straight line about points of SPM concentration of a WTS sample against the mean LBSS voltage obtained by the LBSS at the WTS intake during the WTS sample acquisition (Figure 4). The curve fitting was accomplished using a least squares approach with the added condition that each line pass, at zero SPM concentration, through the point of particle free voltage determined as described above. The mathematical expressions of the calibration curves are displayed in Figure 4.

[16] There are concerns regarding the LBSS calibration that should be noted. One is that the calibration formula for the low-sensitivity LBSS is based on only 9 data points. While the formula for the high-sensitivity LBSS is determined from significantly more data points, these points are broadly scattered about the calibration line (R^2 = 0.5), possibly because of significant temporal variation in the local SPM size distribution. Finally, there are no in situ calibration data acquired during events of relatively high SPM concentration. As a result, application of the calibration formula to LBSS data acquired during such events is based on extrapolation of the calibration curves to SPM concentrations beyond the range of the calibration data.

3.3. Estimating Near-Bottom Wave Velocity and Bottom Stress

[17] Bottom stress was computed according to the scheme outlined by *Grant and Madsen* [1979], which accounts for stress generation by the nonlinear interaction of currents due to surface waves with the more slowly varying flow. The more slowly varying flow is typically referred to as the "steady" flow. In most applications [*Lyne et al.*, 1990b] it is taken as an average flow over some time period that is considerably longer than the dominant surface wave period, but shorter than the periods of other dominant types of fluctuating currents such as inertial waves and tides.

[18] A parameter required by the Grant and Madsen scheme is the relative angle between the steady current and the wave current directions. Unfortunately, our data sets do not include wave directional information. All the bottom stresses displayed here have been computed with the assumption that the wave-induced and steady currents are colinear. For a given set of wave and steady current velocity magnitudes, this produces the maximum stress [see *Grant and Madsen*, 1979, Figure 4]. For the wave and steady current magnitudes used in our stress calculations, the bottom stresses computed by assuming colinear wave and steady currents are roughly 0–40% larger than stresses computed with the assumption of perpendicular wave and steady current directions.

[19] Other parameters required to implement this scheme include physical bottom roughness (section 4.4), the steady flow magnitude at a specified distance above the bottom, and a characteristic amplitude and period of the near-bottom

orbital wave velocities. A stress was calculated for each 8.5-min burst sampling interval. The steady flow was taken as magnitude of the burst-averaged velocity at the lowest BASS current meter (at 0.3 m above bottom (mab) on one tripod and 0.4 mab on the other). The characteristic amplitude and period of near-bottom wave velocities during each sampling interval were determined by two methods, the choice depending on the availability of near-bottom pressure data.

[20] Using data sets that included pressure measurements, the required wave properties of each sampling interval were determined by first converting burst pressure measurements to a spectrum of orbital wave velocities using linear wave theory [*Cacchoine et al.*, 1987; *Lyne et al.*, 1990b] The characteristic orbital velocity amplitude, *Uo*, was then computed from:

$$Uo = 2\sqrt{\int S(f)df} \tag{1}$$

where, $S(f)$ is the orbital wave velocity spectral estimate at frequency *f*. According to *Longuet-Higgins* [1952] this is roughly equal to the mean of the strongest 1/3 of the orbital wave velocities represented in the spectrum. The characteristic orbital frequency, *fo*, was computed as a weighted average over the spectra; i.e.,

$$fo = \int fS(f)df \Big/ \int S(f)df \tag{2}$$

Despite repeated repair efforts, the pressure sensor on the deeper of the BASS tripods always malfunctioned. Calculation of wave properties at these deeper tripod locations was done using the BASS burst velocity measurements. This was a less attractive alternative to using pressure measurements. Near-bottom high-frequency pressure fluctuations are primarily due to surface waves, whereas near-bottom high-frequency velocity fluctuations have other possible sources, including turbulence. Using the BASS velocity data, estimates of characteristic orbital wave velocity and frequency were calculated according to:

$$Uo = 2\sqrt{\int_{fl}^{fu} S_v(f)df} \tag{3}$$

and

$$fo = \int_{fl}^{fu} fS_v(f)df \Big/ \int_{fl}^{fu} S_v(f)df \tag{4}$$

Where S_v is the spectrum of near-bottom velocity magnitude defined as

$$S_v = S_N + S_E \tag{5}$$

in which S_N and S_E are the spectra of the east and north velocity components, respectively, of a sampling burst. Assigning values to f_l and f_u was done with the goal of confining the integration interval above to the frequency band over which the near-bottom currents were predominantly the product of surface wave motion. This was accomplished by comparing curves of S and S_v determined from coinciding measurements of pressure and velocity. The resulting choice of values (f_l = 0.07 and f_u = 0.27 Hz) corresponds to a period range of 3.8–14.2 s. Using these limits, values of *Uo* computed from velocity data show good agreement with *Uo* computed from coincident pressure measurements (obtained on the same tripod), differing by less than 1 cm s^{-1} at Uo > 2 cm s^{-1}.

4. Results

4.1. Seasonal Cycle of Near-Bottom Temperature and Water Velocity

[21] The 1999 time series data from the outer shelf (22-m) and middle slope (60-m) tripods (Figure 5) reveal three distinct near-bottom temperature and current regimes, each nearly coinciding with a tripod deployment period. For convenience, these periods are referred to as the spring, summer and autumn deployments, although they do not strictly coincide with these seasons.

[22] Measurements of the spring deployment (mid-April through mid-June) show near-bottom water over the shelf and slope to be relatively cold, <9°C. These measurements also show subinertial currents that are highly correlated in the across-isobath direction. In particular, the subinertial alongshore currents seen at the 22-m and 60-m sites are nearly identical throughout the spring deployment. They fluctuate from a northeastward to a southwestward direction with a period of 5–10 days. These currents are also highly coherent, and appear to be driven predominantly by the alongshore component of the surface wind stress.

[23] Differences between the outer shelf and middle slope environments, rather than similarities, are apparent in data of the summer deployment (late June through mid-August). At 60 m, near-bottom temperatures are relatively cold, mostly <8°C, and near-bottom currents are weak, mostly <10 cm s^{-1} in magnitude, throughout the summer deployment. By contrast, measurements at 22 m over this period show the frequent appearance of warm water, >10°C, moving at a rapid rate, >20 cm s^{-1}, to the northeast. Such events appear to occur in response to northeastward (downwelling favorable) alongshore winds. Accordingly, the near-bottom cross-shore currents tend to be predominately offshore during these events. A reasonable interpretation is that the downwelling winds of the summer deployment generate a circulation that carries warm water, associated with the Keweenaw Current, to the outer shelf but not as far offshore as the middle slope. Also apparent in the summer deployment data is evidence of an upwelling event in mid-August generated by a strong southwestward wind. This is presumably responsible for the appearance of cold, near 4°C, water at the 22-m isobath.

[24] Data of the autumn deployment (mid-August through late October) show frequent episodes in which downwelling favorable winds coincide with the appearance of warm water and strong northwestward flow over the upper slope. This change in the near-bottom slope environment, from near quiescence in the summer to a regime marked by episodic appearance of the Keweenaw Current during

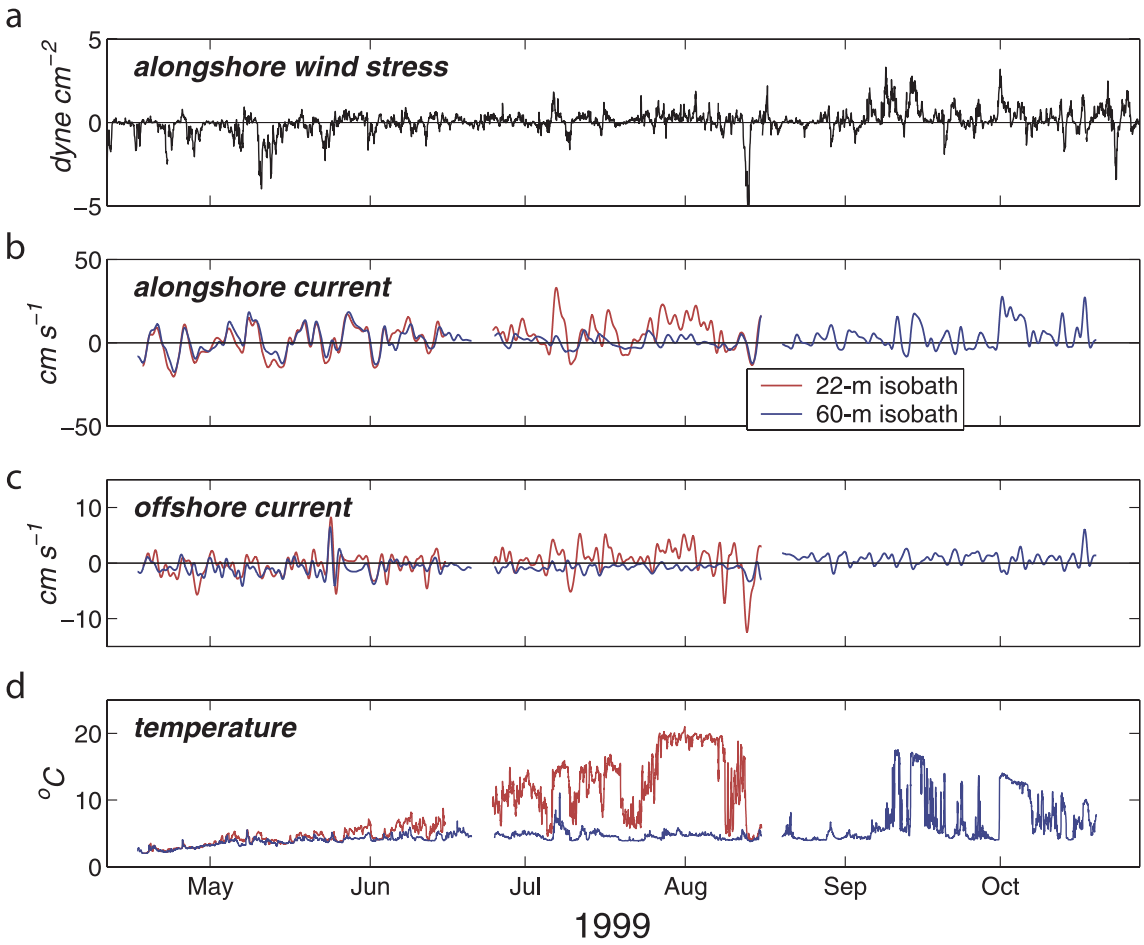

Figure 5. For the 1999 tripod deployments, near-bottom temperatures measured at the (d) 22- and 60-m isobaths, subinertial (b) alongshore and (c) offshore velocities measured at the same isobaths, and (a) estimated alongshore wind stress determined from wind velocity measurements at buoy 45006. Alongshore (offshore) velocities are positive to the northeast (offshore).

autumn, is likely due in part to the seasonal evolution of the wind field over central Lake Superior. Our calculations indicate that the three most prominent downwelling favorable wind events of the summer 1999 deployment have peaks in alongshore surface wind stress in the range of 1.8–2.2 dyne cm^{-2}. By contrast, the maxima in alongshore wind stress of the three most prominent downwelling wind events of the autumn 1999 deployment range over 2.8–3.2 dyne cm^{-2} (see Figure 5).

[25] The 2000–2001 data from 60 and 90 m (Figure 6) show essentially the same seasonal pattern as seen in the 1999 data, with two fairly distinct temporal regimes in flow over the slope. The August 2000 data show what may be characterized as the "summer regime" with predominately cold and slow moving water over the middle and lower slope. As in 1999, this is followed by an "autumn regime" marked by frequent episodes in which warm water moving rapidly to the northeast appears over the slope in conjunction with downwelling favorable alongshore winds. Particularly strong northeastward currents, with magnitudes >20 cm s^{-1}, are evident in the data of the second deployment of 2000–2001 (late October 2000 through mid-January 2001). Their extension to the lower slope, as far as the 90-m site, may be taken as further indication of a seasonal expansion of the Keweenaw Current.

[26] Further details of the seasonal current regimes seen over the outer shelf and upper slope are revealed by examining the spectra of near-bottom velocities of each of the 1999 deployments (Figure 7). Spectra of the spring deployment velocities show near-bottom energy levels over the slope and outer shelf to be comparable over all frequencies. This contrasts with spectra of summer deployment velocities, which show an order of magnitude difference over all frequencies between the energy of currents over the slope and the energy of the far more vigorous currents over the outer shelf. At periods of less than 30 days, outer shelf currents of the summer deployment are actually far more energetic than the outer shelf currents of the spring deployment. Over the slope, energy levels in all frequency bands are strongest during the autumn deployment.

4.2. Contribution of Internal Wave Motion

[27] Of particular interest is the influence of high-frequency motion on the total variance of our measured velocities. Studies in a number of locations have shown that near-inertial currents and higher-frequency motions in

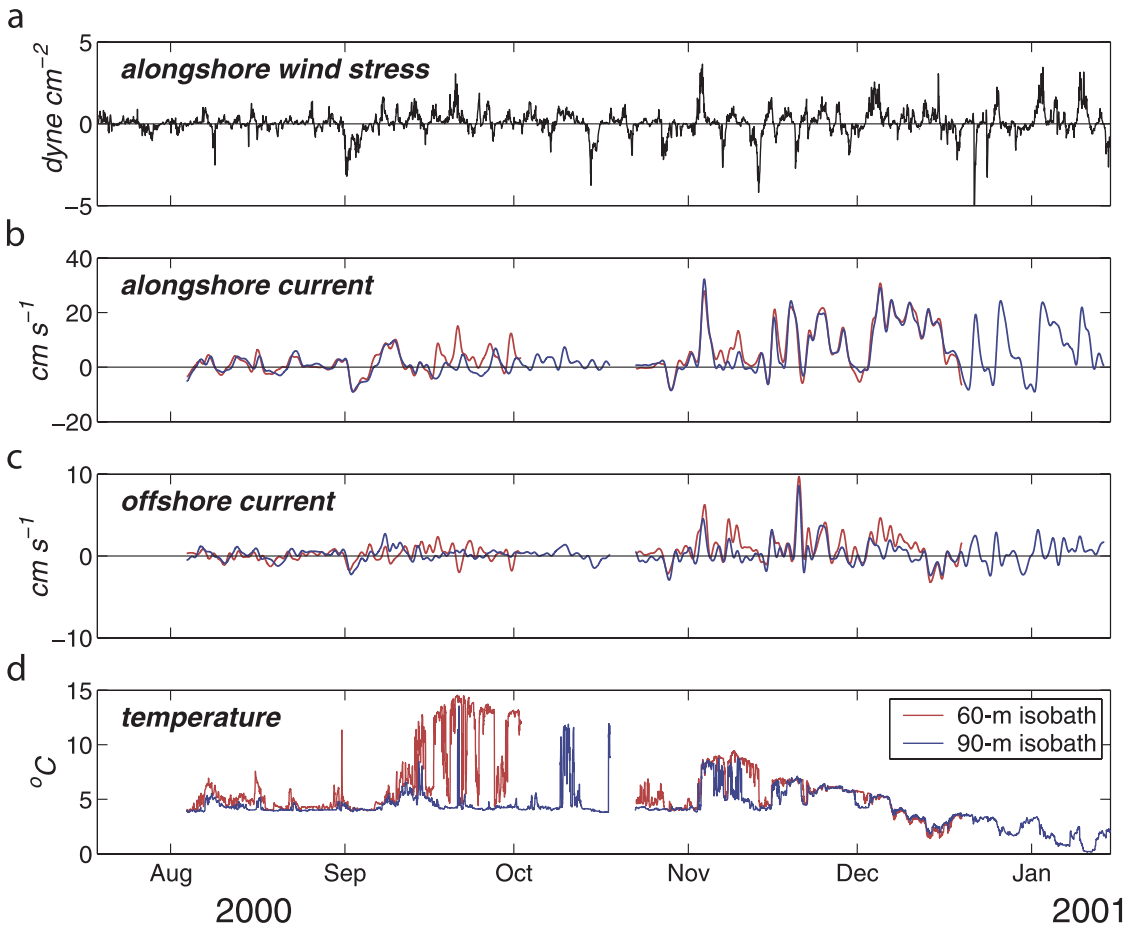

Figure 6. Same as Figure 5, except showing properties measured during 2000–2001 and alongshore wind stress computed using wind measurements from the Devils Island C-MAN station.

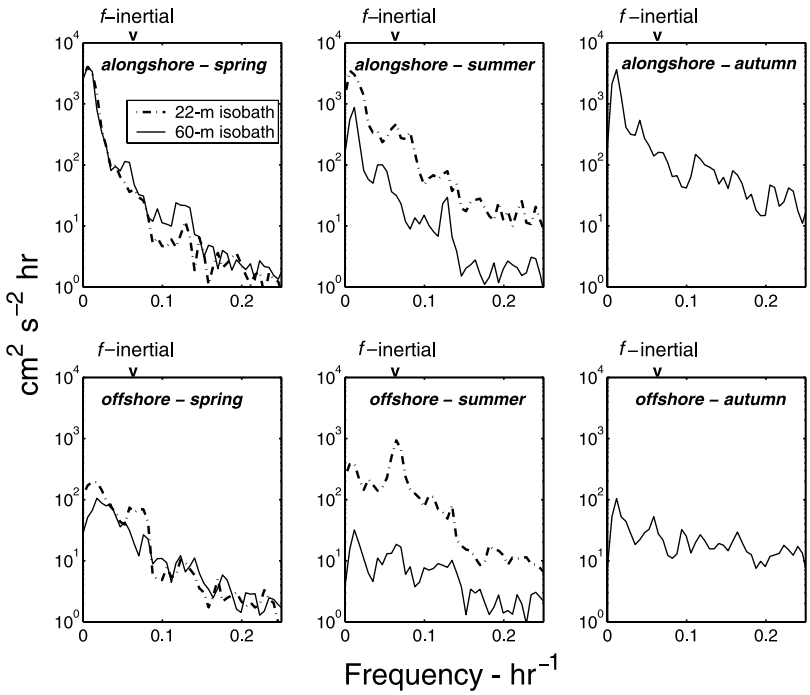

Figure 7. Spectra of near-bottom alongshore and offshore velocities measured 4.5 mab at the 22- and 60-m isobaths during the spring, summer, and autumn deployments of 1999. The marks on the upper axes indicate the local inertial frequency.

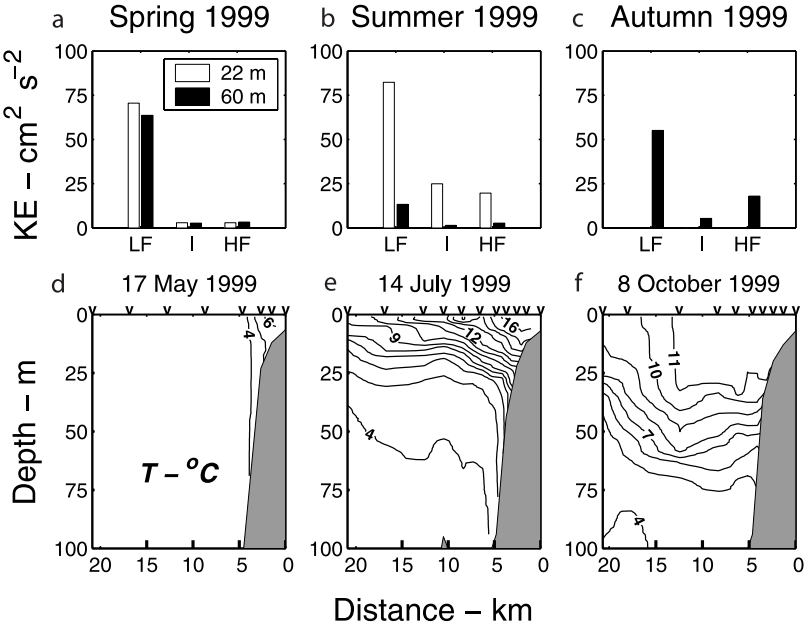

Figure 8. (a)–(c) The total kinetic energy per unit mass, separated into three frequency bands, of the velocities measured at the uppermost BASS current meter and at the indicated location during the 1999 deployments. The band designations are LF, low frequency; I, inertial; and HF, high frequency (see text for band ranges). (d)–(f) Sample temperature distributions measured in our study area for the deployment periods of the kinetic energy plots directly above.

the internal wave band can significantly contribute to the strength of near-bottom currents over shelf edge and slope regions [*Csanady et al.*, 1988; *Flagg*, 1988; *Churchill et al.*, 1994; *Bogucki et al.*, 1997]. The velocity spectra from a number of our deployments show a peak near the inertial frequency, most notably the spectra of velocities measured at the shelf edge during the summer deployment of 1999 (Figure 7). To more fully examine the contribution of high-frequency motions on the near-bottom velocity variance in our study region, we have divided the velocity variance of our various deployments into three frequency bands. These are a low-frequency band (encompassing periods of 19–171 hours), an inertial band (13–19-hour periods) and a high-frequency band (0.7–13-hour periods). Note that the inertial period at our study site (47.25°N) is 16.3 hours.

[28] Displayed here (Figure 8) is the sum of the individual component velocities (e.g., alongshore and offshore) variances in each of the frequency bands for the 1999 deployments. Hereafter, we refer to these as kinetic energies, although they are technically the kinetic energy per unit mass, times a factor of two, within each of the designated frequency bands. In view of the required link between vertical stratification and internal waves, these values show a temporal variation of internal wave energy that relates to the evolving lake temperature field in a manner that would be expected. This is nicely illustrated by comparing the kinetic energies of 1999 deployments with sample across-shore temperature distributions from these deployments (Figures 8d–8f).

[29] The across-shore temperature distributions acquired during the 1999 spring deployment show little vertical temperature stratification over the shelf edge and outer slope of our study area (e.g., Figure 8d). Accordingly, the spring deployment velocity records have very little energy in the inertial and higher-frequency bands (Figure 8a).

[30] By contrast, temperature distributions measured during the 1999 summer deployment show a well developed thermocline intersecting the bottom over the shelf edge (Figure 8e). The resulting large vertical stratification over the shelf edge appears to support vigorous near-inertial and higher-frequency motions as revealed by the band-segregated kinetic energy levels from the 22-m velocity records of the summer deployment (Figure 8b). For the 4.5-mab velocity record, for example, 35% of the total kinetic energy is contained in the inertial and high-frequency bands. The summer deployment data further show water of the thermocline (>6°C) seldom extending to the middle slope (Figures 8b and 8e and Figure 5d). The shallow thermocline of summer apparently isolates near-bottom water of the midslope from wind-driven near-surface flows, as indicated by the very low kinetic energy levels seen in all frequency bands of the summer deployment 60-m velocities.

[31] During the autumn 1999 deployment, the thermocline and vigorous near-inertial motions are frequent visitors to the midslope. Evidence of recurrent incursions of the thermocline to the midslope is provided by the autumn deployment temperature data (Figure 5) and confirmed by the across-slope temperature distributions derived from shipboard survey data (Figure 8f). The 60-m velocities of this deployment give the highest levels of inertial and high-frequency band energy of any velocity set from the slope region (from both 1999 and 2000). At 4.5 mab, 30% of the total kinetic energy is contained in the inertial and high-frequency bands. At the lowest current meter level, 0.4 mab,

Table 1. For the Band Encompassing Periods of 1.6–14 Days, Squared Coherence and Phase Relating Alongshore and Across-Shore Velocity at the Uppermost BASS Current Meter With Alongshore Wind Velocity Measured at NOAA Buoy 45006 (in 1999) and at the Devils Island C-MAN Station (in 2000)[a]

		Alongshore Velocity		Across-Shore Velocity	
Isobath	Period	Squared Coherence	Phase, deg	Squared Coherence	Phase, deg
22	17 April to 15 June 1999	0.78	43	0.10	
22	24 June to 15 Aug. 1999	0.54	51	0.34	−9
60	16 April to 20 June 1999	0.61	51	0.09	−29
60	25 June to 15 Aug. 1999	0.04		0.19	23
60	19 Aug. to 19 Oct. 1999	0.15	74	0.17	−46
60	3 Aug. to 3 Oct. 2000	0.24	46	0.3	
60	22 Oct. to 19 Dec. 2000	0.24	49	0.15	26
90	3 Aug. to 18 Oct. 2000	0.16	61	0.28	−13
90	22 Oct. to 31 Dec. 2000	0.20	42	0.14	19

[a]These values were calculated by spectral analysis [*Bendat and Piersol*, 1971] through piece averaging (341-hour piece length) and band averaging over the above period band. Positive phase indicates wind leading water velocity. Phase is given only where squared coherence exceeds the 99% significance level. Isobaths are in meters.

the proportion of inertial plus high-frequency band kinetic energy increases to 40%.

4.3. Relationship of Near-Bottom Currents and Wind

[32] Results of cross-spectral analysis indicate a strong influence of winds on near-bottom motions over the slope and outer shelf during all seasons. Shown here (Table 1) are coherences and phases, averaged over a 1.6–14-day period band, relating the alongshore and across-shore components of near-bottom velocity measured during each deployment with the alongshore component of wind velocity. With few exceptions, the coherences are significant at the 99% confidence level. The phases are consistent with the expected nearshore response to the alongshore wind. In the selected frequency band, alongshore currents lag the alongshore wind by phases of between 43° and 74°, consistent with acceleration of the alongshore current by the alongshore wind. The small phase difference between the alongshore wind and across-shore currents conforms with an upwelling/downwelling response to the wind, with northeastward (southwestward) winds generating offshore (onshore) near-bottom flow.

4.4. Bottom Roughness

[33] According to the theory of *Grant and Madsen* [1979], the bottom boundary layer may be divided into nested sublayers. Near the bottom is a thin (order 10-cm-thick) layer in which stress generation is due to the nonlinear interaction of orbital velocities due to surface waves and the more slowly varying "steady current". Stress in the layer above is principally due to turbulence generated by vertical shear of the steady current. The velocity profile in this "constant stress" layer may be approximated as:

$$u = \frac{u_*}{k} \ln(z/z_0) \tag{6}$$

where z is distance above bottom, k is von Karmen's constant (assumed to be 0.4), z_0 is the effective bottom roughness and u_* is the friction velocity, taken as $u_* = \sqrt{\tau/\rho}$ where τ is shear stress and ρ is water density.

[34] In the presence of near-bottom wave motions, z_0 is a nonlinear function of the orbital wave velocity and steady current velocity. In the absence (or near absence) of near-bottom wave motions, the value of z_0 reflects the response of the steady flow to the roughness of the bottom. For fully rough turbulent it can be related to physical bottom roughness, k_b, through [*Nikuradse*, 1933]

$$z_0 = k_b/30. \tag{7}$$

In theory then, the physical bottom roughness, k_b, may be determined from near-bottom steady current profiles acquired during periods of near-zero orbital wave motions at the bottom. Following this reasoning, we estimated k_b according to equations (6)–(7) using profiles of velocities averaged over sampling bursts with characteristic orbital wave velocity, *Uo*, of less than 2 cm s^{-1}. In an attempt to ensure that the conditions implicit in equation (6) were satisfied, we further restricted the profiles used to determine z_0. Because the height of the constant stress layer should be expected to vary with steady current magnitude at some level, we excluded profiles in which midlevel burst-averaged velocity magnitudes (at the third or fourth highest BASS current meter) were less than 15 cm s^{-1}. Because equation (6) assumes a vertically constant density, profiles acquired during bursts in which the averaged temperatures near the top and base of the BASS tripod differed by more than 0.2°C were also excluded. Further eliminated from the analysis were profiles in which orientations of the burst-averaged velocities varied by more than 5°. Finally, profiles not closely conforming to the mathematical form of equation (6) were excluded by requiring that the standard error of u_*, determined by least squares fit of u to ln(z), be less than 0.1 cm s^{-1} (Figure 9).

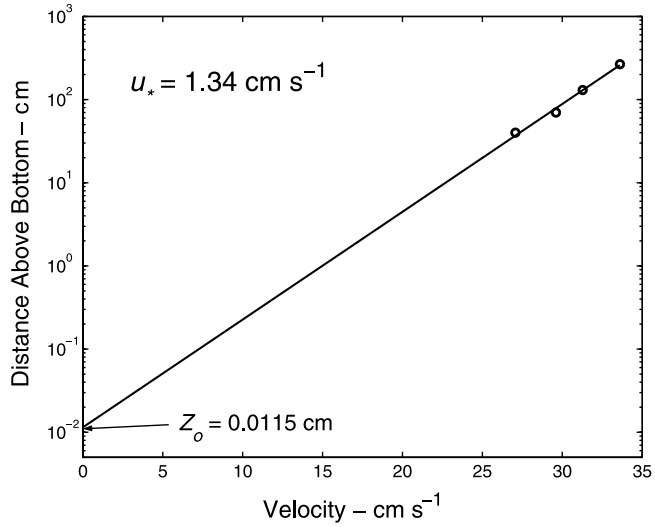

Figure 9. Example of a vertical profile of burst-averaged velocity acquired during a period of near-zero orbital wave motion near the bottom. The line is the least squares linear fit of the averaged velocities (circles) against log of height above bottom. The values of u_* and z_o are determined according to equation (6).

Table 2. Estimates of Bottom Roughness, k_b, Determined From Equations (6)–(7), Using N Number of Velocity Profiles Acquired at the Indicated Water Depth and Year[a]

Year	Water Depth, m	N	k_b, cm
1999	22	368	3.15 ± 0.15
1999	60	23	0.57 ± 0.08
2000	90	100	0.57 ± 0.06

[a]Error intervals are the standard errors about the means.

[35] With these restrictions, the number of profiles from which z_0 could be determined in the near absence of orbital wave motion is small (Table 2). As a result, no temporal changes in k_b, which may be expected as a result of storm action on the bottom, could be discerned. Nevertheless, the ensembles of k_b give a statistically robust average at each of the tripod depths (Table 2), exceeding its standard error by at least a factor of 6. These averages suggest that the bottom roughness over the outer shelf may be significantly higher (by roughly a factor of 5) than bottom roughness over the slope.

[36] A number of factors may contribute to physical bottom roughness. These include the roughness of individual sand grains [*Nikuradse*, 1933], the roughness associated with bottom bed forms [*Grant and Madsen*, 1982] and the flow resistance due to very near bed particle transport [*Wiberg and Rubin*, 1989]. The contribution of individual sand grains may be assessed through properties of the bottom grain size distribution. A useful property is D_N, the diameter that exceeds some percent, N, of the sediment grain diameters. Analysis of sediment samples from our study region give values of D_{90} no greater than 0.05 cm, considerably smaller than our estimates of k_b over either the slope or shelf edge (Table 2). Bottom roughness of our study region is thus principally due to factors other than the resistance to flow offer by individual sand grains. As indicated by studies in other regions, roughness elements associated with bottom bed forms are likely significant contributors to bottom roughness [*Cacchoine et al.*, 1987; *Lyne et al.*, 1990a; *Xu and Wright*, 1995; *Traykovski et al.*, 1999].

4.5. Bottom Wave and Stress Climate

[37] Our measurements indicate that storm-driven surface waves within Lake Superior tend to have relatively short periods as compared with waves in the open ocean. During episodes of elevated wave energy, characteristics wave periods computed from the BASS pressure measurements (as described in section 3.3) are predominately in the 6–9 s range. By contrast, near-bottom wave velocities with periods exceeding 12 s are commonly seen in the open ocean [e.g., *Lyne et al.*, 1990a; *Sherwood et al.*, 1994]. According to linear wave theory, the motion of the relatively short waves seen in Lake Superior should decay more rapidly with depth than their longer period oceanic counterparts.

[38] Nevertheless, our measurements reveal vigorous near-bottom wave motions at the Keweenaw shelf edge. The 22-m BASS tripod measurements, which encompass the 1999 spring and summer deployments but not the stormier autumn deployment, show frequent episodes during which characteristic near-bottom orbital wave velocities exceed 10 cm s^{-1} (Figure 10). At 60 m, characteristic wave velocity magnitudes are expectedly much smaller. Throughout the spring and summer deployments of 1999, orbital wave velocities observed at 60 m never exceed 1.5 cm s^{-1}. During the deployments of autumn and winter, much higher orbital wave velocities are indicated by the 60-m data. They attain maximum values of 5 cm s^{-1} during the autumn 1999 deployment (Figure 11) and 9 cm s^{-1} during the second 2000–2001 deployment (not shown). At 90 m, observed wave currents are always weak. Nevertheless, they also exhibit a seasonal signal, with characteristic amplitudes not exceeding 0.8 cm s^{-1} during the first deployment of 2000–2001, but peaking over 1.3 cm s^{-1} on three occasions during the ensuing deployment (Figure 12).

[39] To assess the impact of wave motions on bottom stress generation, we have computed bottom stress using the theory of *Grant and Madsen* [1979] with and without the inclusion of surface wave currents. The results indicate that surface wave currents significantly enhance bottom stress generation at the Keweenaw shelf edge. During several storms, stresses computed using the 22-m tripod data increase by an order of magnitude with the inclusion of surface wave currents (Figure 10). The indicated increase in bottom stress due to surface wave currents at 60 m is much less. Nevertheless, this increase exceeds a factor of 50% on seven separate occasions: three in 1999 (Figure 11) and four in 2000. It is greater than 100% during three of these events. Even over the lower slope, wave currents appear to have some impact on bottom stress generation. Inclusion of surface wave motion increases computed bottom stress at the 90-m isobath by more than 20% on four separate occasions, all during the second deployment of 2000–2001 (Figure 12). From analysis of measurements acquired off the northern tip of the Keweenaw Peninsula, *Hawley* [2000] also found that current due to surface waves appreciably contribute to bottom stress generation at 90-m depth during the winter and late autumn.

[40] Our calculations also indicate frequent occurrence of large bottom stresses over the Keweenaw slope during some periods. Particularly notable is that bottom stress computed from the 90-m data exceeds 2 dyne cm^{-2} on 11 separate occasions (Figure 12). That these all occur during the second of the 2000–2001 deployments (mid-October 2000 through mid-January 2001) indicates that generation of high bottom stress over the lower slope may be a seasonal phenomenon, restricted primarily to winter and late autumn.

4.6. Impact of High-Frequency Motions on Bottom Stress Generation

[41] As noted above, high-frequency motions in the internal wave band can significantly contribute to near-bottom kinetic energy during periods when near-bottom waters are vertically stratified. To examine the effects of high-frequency motions on bottom stress generation, we have computed bottom stress series with these motions largely eliminated. This was accomplished by using low-pass-filtered velocity component series, generated with use of a 33-hour half-power point filter, to create the near-bottom current speed series for use in the Grant-Madsen methodology.

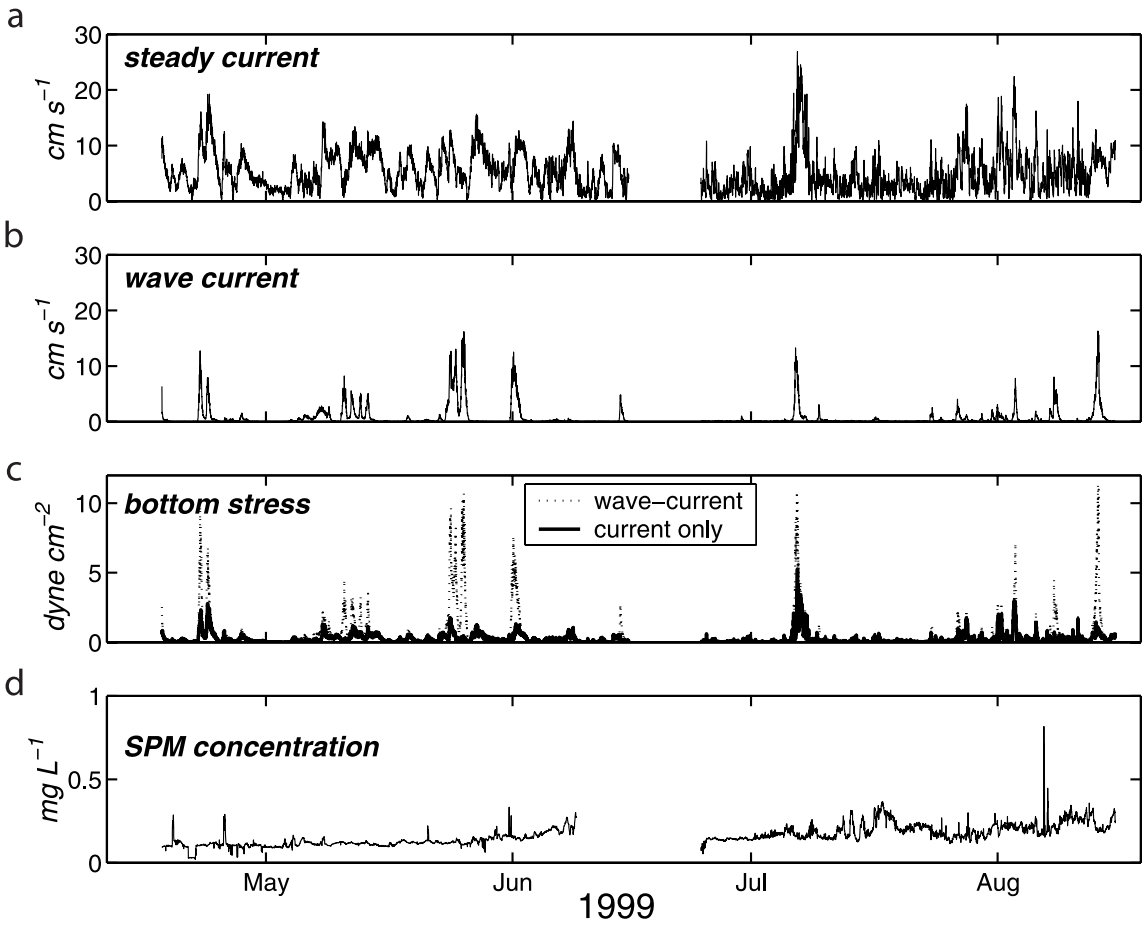

Figure 10. Time series derived using measurements from the BASS tripod sensor array at the 22-m isobath. Shown are the (a) burst-averaged near-bottom velocity magnitude, (b) characteristic amplitude of near-bottom orbital wave motion, (c) computed bottom stresses, and (d) estimated SPM concentration (at 0.4 mab). One bottom stress series shown was computed with the action of surface wave currents included (dashed line, Figure 10c), and the other was computed with orbital wave motion amplitude set to zero (solid line).

[42] To examine the maximum effect of high-frequency motions on stress generation over the slope, we concentrate here on the stress series computed from the 60-m data from the autumn 1999 deployment. Of all slope velocity sets, these gave the highest proportion of kinetic energy in the internal wave band (section 4.2). For all events of high bottom stress, the stresses computed from the unfiltered velocity data of this deployment are much greater than the stresses compute with the filtered velocity data. In the illustration shown here (Figure 13), the stress computed from the unfiltered velocities exceeds its counterpart determined from filtered velocities by more than 2.5 dyne cm^{-2} on two occasions, one on 1 October and the second on 13 October. For the entire deployment period, there are 30 separate occasions when the stress computed from the unfiltered velocities surpasses 1.5 dyne cm^{-2}. For these, the stress computed from the unfiltered velocities exceeds the filtered velocity-derived stress by an average value of 1.0 dyne cm^{-2} and an average factor of 2.1. Clearly, high-frequency motions significantly enhance bottom stresses over the Keweenaw slope during periods when the seasonal thermocline intersects the slope.

4.7. Sediment Resuspension

[43] Comparison of the SPM concentration and bottom stress time series (Figures 10–12) reveals clear spatial and temporal patterns of sediment resuspension over the Keweenaw slope and outer shelf. Despite frequent events of high bottom stress at the outer shelf, there is no clear evidence of local sediment resuspension at 22 m (Figure 10). This is undoubtedly due to the small fraction of fines within the outer shelf bottom sediment (Figure 3). It is possible that fines are resuspended at the outer shelf during the period of our measurements, but not at quantities sufficient to produce a clear signal in the LBSS records.

[44] Local sediment resuspension over the slope appears to be confined primarily to autumn and winter. For example, the 60-m time series of 1999 (Figure 11) reveal several events of local sediment resuspension, marked by coincident high values of bottom stress and SPM concentration, during the autumn deployment, but show no such events

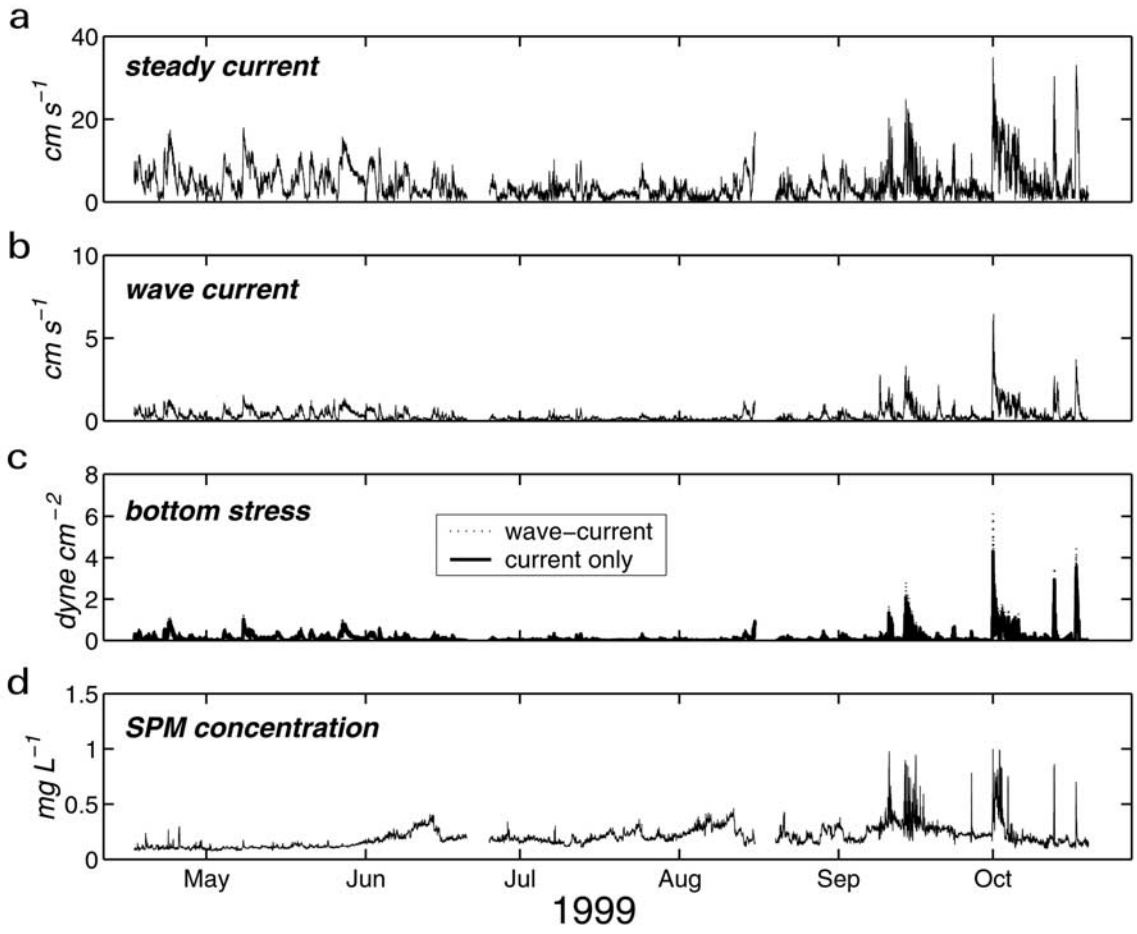

Figure 11. Same as Figure 10, except showing time series determined using measurements from the BASS tripod sensor array at the 60-m isobath.

during the spring and summer deployments. At the lower slope, the 90-m time series of 2000–2001 (Figure 12) offer no evidence of local resuspension until an early November event of significant bottom stress and elevated SPM concentration. A number of episodes of high bottom stress (>2 dyne cm^{-2}) with a modest rise in SPM concentration (up to 0.3–0.7 mg L^{-1}) are observed following this event.

[45] Among the parameters required for modeling sediment movement is the resuspension threshold, the minimum stress at which the bottom sediment is resuspended [e.g., *Lyne et al.*, 1990b; *Harris and Wiberg*, 2001; *Li and Amos*, 2001]. Determination of resuspension thresholds from coincident bottom stress and SPM time series is a process complicated by effects of horizontal advection of turbid water to the measurement site. For our time series, it is also complicated by the data gaps between the burst samples, as resuspension events often appear to be initiated within these gaps. In such circumstances, two burst-averaged stresses bracket the beginning of a resuspension event. These then define a range of bottom stress within which the actual resuspension threshold is presumably embedded.

[46] From visual examination of the bottom stress and SPM time series, we subjectively determined the stresses bracketing the initiation of clear resuspension events: those episodes in which bottom stress and SPM concentration rose sharply at the same time. This analysis was restricted to what we deemed major resuspension events, those with SPM concentration greater than 0.4 mg L^{-1}, and to those occurring after a period of three days with no clear local sediment resuspension. Our analysis was further restricted to two sets of time series: those derived using the 1999 autumn deployment data from 60 m and those determined using the data of the second 2000–2001 deployment from 90 m. Both sets of series show a period with frequent resuspension events, which occurs following a lengthy time (>1 month) of no clear evidence of local resuspension (Figures 11 and 12).

[47] Though they must be viewed with some caution, the results (Table 3) indicate a tendency for the resuspension threshold to increase with successive resuspension events. For example, the results derived from the 1999 60-m data indicate resuspension thresholds increasing from less than 1 dyne cm^{-2} during September to more than 1.5 dyne cm^{-2} during October. The results determined from the 2000 90-m data are less well defined. Nevertheless, they indicate a relatively low threshold for the initial resuspension event of autumn (<0.36 dyne cm^{-2}) and much higher thresholds for the subsequent events. It is highly possible that such a temporal increase in resuspension threshold could be the result of bed armoring, the removal of easily resuspended

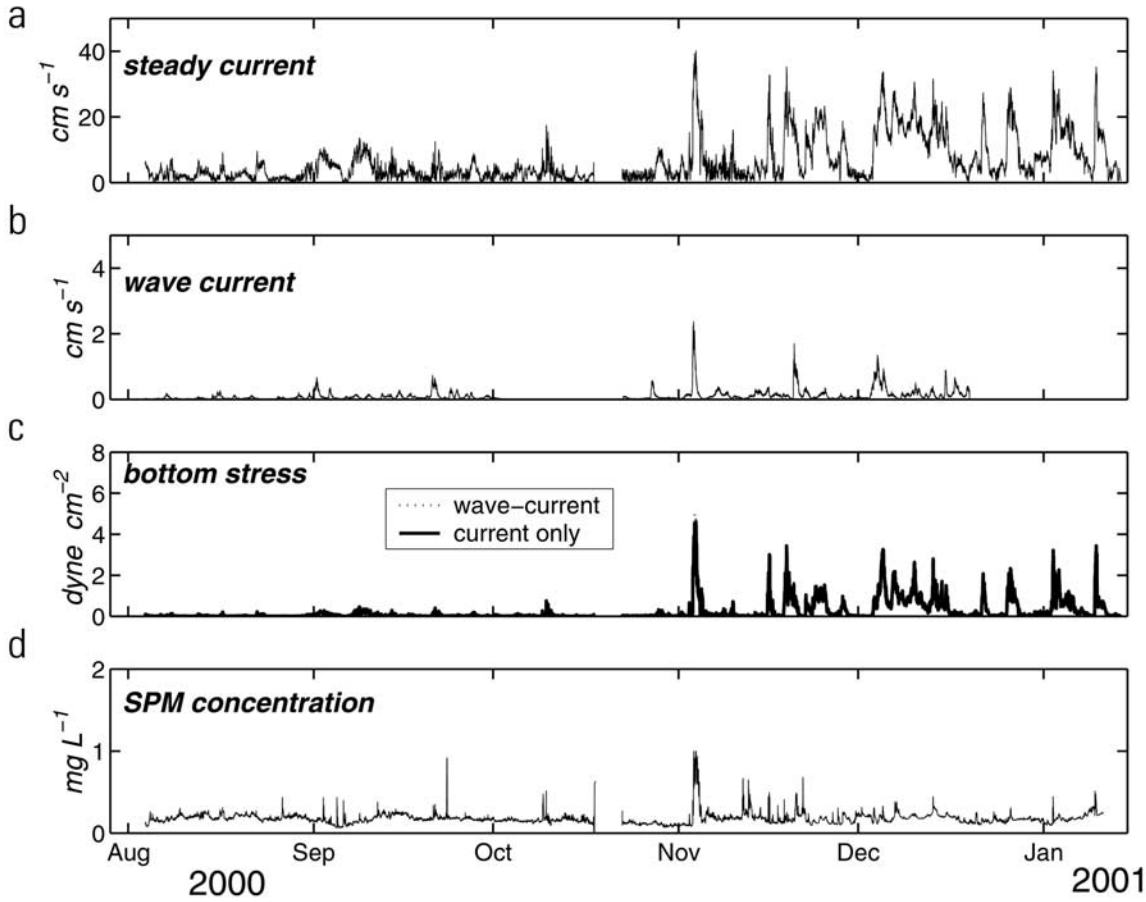

Figure 12. Same as Figure 10, except showing time series determined using measurements from the BASS tripod sensor array at the 90-m isobath.

bottom material, through the series of autumn and early winter resuspension events.

4.8. Sediment Transport

[48] Placement of the LBSSs and BASS current meters at identical vertical levels enables computation of SPM flux as the product of velocity and LBSS-derived SPM concentration. These flux estimates are admittedly plagued by a number of uncertainties, many of which are not easily quantified. They include uncertainties in SPM concentration due to imperfect calibration of the LBSS signal and potential errors in velocity due to misalignment of the local coordinate system. The latter is particularly important when considering across-shore SPM fluxes, as it is common for a small change in the orientation of the cross-shore axis to significantly alter the across-shore velocity component. Nevertheless, the estimated flux series allows us to examine the conditions under which events of significant sediment transport occur.

[49] As with the contributing velocity and SPM concentration series, the SPM flux series exhibit clear seasonal patterns, with distinct regimes nearly confined to deployment periods. Consider, for example, the 1999 flux series at the 60-m isobath (Figure 14). During the spring deployment, both the alongshore and offshore SPM flux components at 60-m fluctuate about zero. This is an upshot of the wind-dominated current regime of the period marked

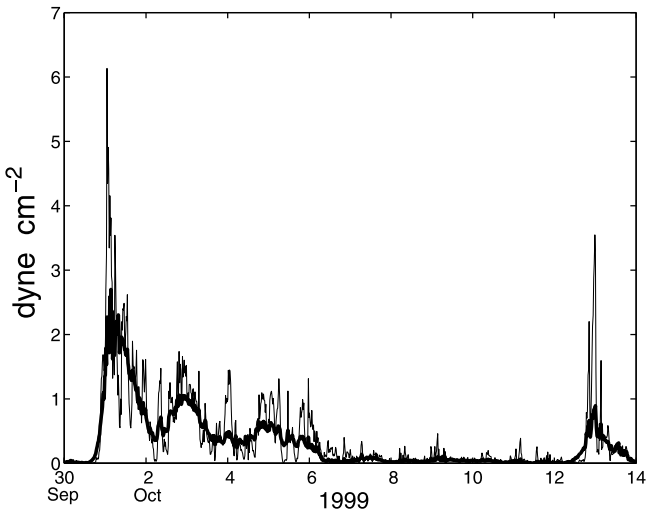

Figure 13. Comparison of bottom stresses computed from unfiltered velocities measured at the 60-m isobath (thin line) with a bottom stresses computed from the same velocity series but filtered to eliminate high-frequency motions (bold line).

Table 3. Bottom Stresses Observed Just Prior to and After the Initiation of a Sediment Resuspension Event Generated by Bottom Stress at the Given Isobath and Date[a]

Isobath, m	Date	Bracketing Stresses, dyne cm^{-2}
60	10 Sept. 1999	0.55–0.91
	13 Sept. 1999	0.41–0.63
	30 Sept. 1999	0.26–0.42
	12 Oct. 1999	1.62–1.71
	17 Oct. 1999	1.66–2.29
90	2 Nov. 2000	0.11–0.36
	15 Nov. 2000	1.27–1.87
	28 Nov. 2000	0.56–0.97
	13 Dec. 2000	1.46–2.22
	2 Jan. 2001	0.45–1.81
	9 Jan. 2001	0.90–1.10

[a]Hypothetically, the two stresses listed for each event bracket the actual threshold for sediment resuspension.

by alternating upwelling and downwelling flow events (section 4.1). Throughout most of the summer deployment, SPM fluxes at 60 m are uniformly low, a reflection of the predominately weak near-bottom slope currents of the summer period. The exception is a period of relatively large fluxes occurring during the mid-August episode of strong upwelling favorable winds (Figure 14 and Figure 5). As expected, the cross-shore SPM fluxes of this event are directed onshore. During the autumn deployment, numerous episodes of large SPM fluxes are observed at 60 m. These occur during episodes of strong downwelling favorable winds. Accordingly, the SPM fluxes of these events tend to be directed to the northeast in the alongshore direction and toward offshore in the cross-shore direction.

[50] The SPM fluxes observed over the slope during 2000–2001 show a pattern similar to that of the 1999 fluxes. At the lower slope, the flux series at 90 m (Figure 15) show the transition from uniformly low to episodically high fluxes occurring late in the year, during early November. As in 1999, high SPM fluxes seen over the slope during the autumn and winter of 2000–2001 occur during periods of downwelling favorable winds and are directed to the northeast and offshore.

[51] For each deployment period, we computed mean SPM fluxes at all levels where current meter and LBSS data were available (Table 4). These mean fluxes were divided into advective and eddy components according to:

$$\overline{uC} = \overline{u}\,\overline{C} + \overline{(u-\overline{u})(C-\overline{C})} \tag{8}$$

where u is velocity, C is SPM concentration, and the overbars denote time averaging. The first term on the right is mean advective flux and the last term is the mean eddy flux.

[52] The mean SPM fluxes (Table 4) reflect the spatial and temporal patterns of near-bottom SPM concentrations and velocities discussed above.

[53] At 22 m the mean SPM fluxes of the 1999 spring deployment have magnitudes either smaller than or just slightly above their standard errors. The near-zero mean fluxes of this period are the result of the alternating upwelling and downwelling flow episodes driven principally by the fluctuating alongshore wind stress component (section 4.1). By contrast, means of the 22-m SPM fluxes of the summer deployment, during which warm water of the Keweenaw Current frequently appears at the shelf edge, have magnitudes significantly above their standard errors, and are directed to the northeast and offshore.

[54] Over the slope, the mean SPM fluxes indicate little net transport of suspended particulates during the spring and summer, but show a significant net transport of SPM to the northeast and offshore during autumn and winter. By far, the greatest mean SPM fluxes are those of the second 2000–2001 deployment. All of the significant mean fluxes of the

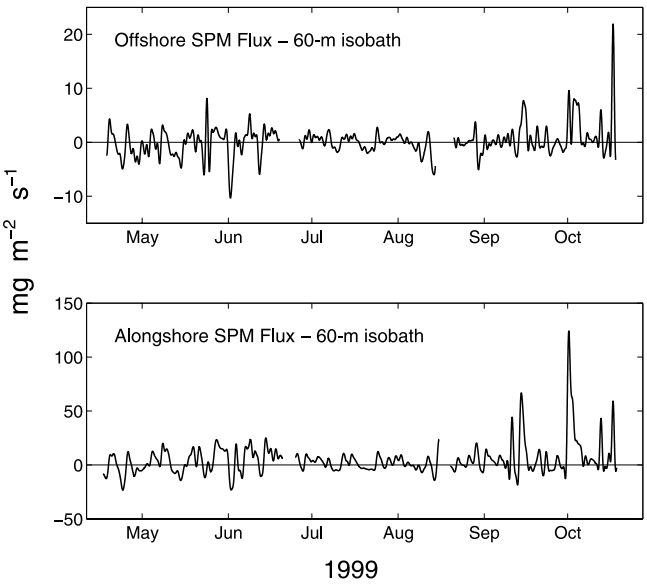

Figure 14. Low-pass-filtered alongshore and across-shore SPM fluxes at 0.4 mab over the 60-m isobath during the three 1999 deployments. Offshore fluxes are positive offshore.

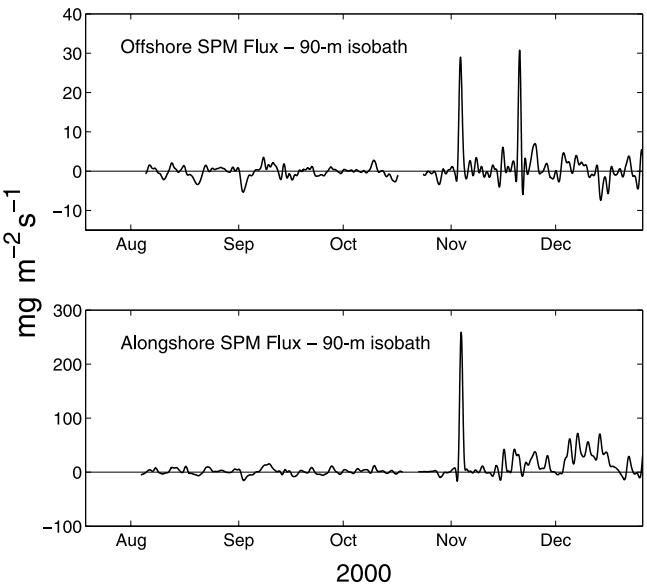

Figure 15. Same as Figure 14, except showing SPM fluxes at 0.4 mab over the 90-m isobath during the two 2000–2001 deployments.

Table 4. Estimated Means and Standard Errors of Sediment Flux at the Indicated Isobath and Height Above Bottom[a]

Isobath, m	Height, mab	Period	Alongshore Means, mg m^{-2} s^{-1}			Offshore Means, mg m^{-2} s^{-1}		
			Total	Eddy	Standard Error	Total	Eddy	Standard Error
22	0.3	17 April to 26 May 1999	−1.3	0.3	2.2	−0.41	0.03	0.24
	0.7	17 April to 26 May 1999	−0.7	1.4	2.8	−0.54	0.24	0.37
	1.3	17 April to 26 May 1999	−1.0	0.7	2.2	−0.33	0.14	0.29
22	0.3	24 June to 7 Aug. 1999	4.7	0.4	1.7	1.31	0.12	0.57
	0.7	24 June to 16 Aug. 1999	3.8	0.2	1.5	1.05	−0.23	0.58
	1.3	24 June to 7 Aug. 1999	7.8	0.2	2.3	2.50	0.29	0.75
60	0.4	16 April to 31 May 1999	1.8	0.3	2.1	−0.45	0.06	0.44
	0.7	16 April to 21 June 1999	1.4	0.1	1.3	−0.00	0.10	0.32
	2.7	16 April to 21 June 1999	2.3	0.6	1.6	−0.40	0.17	0.32
60	0.4	25 June to 15 Aug. 1999	1.4	0.0	0.9	−0.07	0.03	0.15
	2.7	25 June to 15 Aug. 1999	0.4	−0.2	1.1	−0.25	0.03	0.14
60	0.4	19 Aug. to 19 Oct. 1999	9.0	2.9	3.9	0.88	0.28	0.36
	0.7	19 Aug. to 9 Oct. 1999	9.6	2.3	3.9	0.61	0.10	0.34
	2.7	19 Aug. to 19 Oct. 1999	8.4	1.8	3.3	0.36	0.12	0.28
60	0.4	4 Aug. to 2 Oct. 2000	3.4	0.3	1.4	0.66	−0.03	0.22
	2.7	4 Aug. to 2 Oct. 2000	3.6	0.7	1.3	0.16	−0.48	0.19
90	0.4	3 Aug. to 18 Oct. 2000	1.3	−0.0	0.7	−0.18	−0.03	0.13
90	0.4	22 Oct. to 25 Dec. 2000	15.9	3.4	4.4	0.95	0.43	0.32
	0.7	22 Oct. to 25 Dec. 2000	18.5	3.5	5.1	2.12	0.51	0.39
	1.3	22 Oct. to 25 Dec. 2000	18.3	3.9	4.9	0.75	0.23	0.35
	2.7	22 Oct. to 25 Dec. 2000	18.5	1.7	4.8	−0.09	0.17	0.33

[a]Standard error was computed as Std. Err. = $SD/(df)^{1/2}$, where SD is the standard deviation of the fluxes about the estimated mean and df are the number of independent flux measurements from which the mean was calculated. The value of df was approximated as T/T_C, where T is the length of the flux series and T_C is the flux series correlation time.

autumn and winter, specifically those of the autumn 1999 deployment and of the second 2000–2001 deployment, have large eddy components which are also directed to the northeast and offshore.

[55] A factor that may be partly responsible for to the mean offshore SPM fluxes of the late season deployments of 1999 and 2000 is the preponderance of downwelling favorable winds during these deployments (Figures 5 and 6). Mean alongshore wind stresses, averaged over the periods for which the deployment mean SPM fluxes were calculated, are downwelling favorable. However, their magnitudes are relatively small, equaling 0.29 dyne cm^{-2} for the autumn 1999 deployment and only 0.036 dyne cm^{-2} for the second 2000–2001 deployment.

[56] Another factor that could be partly responsible for the large mean offshore SPM fluxes of the late season deployments is the manner in which wind-driven flows combine with the non-wind-driven component of the Keweenaw Current. As noted in section 2, and demonstrated by our data (Figures 5 and 6), downwelling favorable alongshore winds tend to accelerate the Keweenaw Current, whereas upwelling favorable winds have the opposite effect. It follows that bottom stress, and the quantity of sediment resuspended, should tend to be greater during wind-driven downwelling, as opposed to upwelling, events.

[57] Such a tendency is clearly indicated by data of the late season deployments of 1999 and 2000. When plotted against alongshore wind stress, values of SPM concentration and bottom stress of these deployments show a marked asymmetry about zero alongshore wind stress, with much higher values of both properties occurring on the downwelling favorable side of the wind stress axis (Figure 16). As would be expected, the greatest SPM fluxes also occur during downwelling favorable winds, and are directed offshore (Figure 16c).

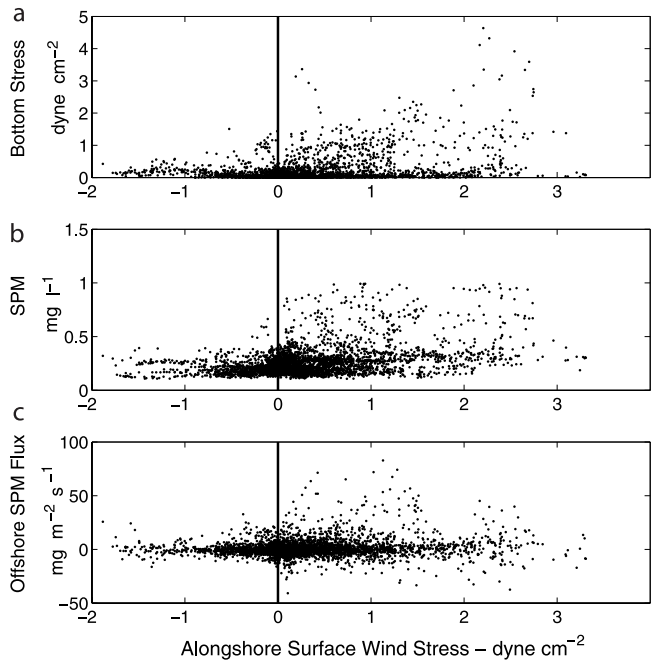

Figure 16. As determined from data acquired at the 60-m isobath during the autumn 1999 deployment, plots of (a) bottom stress, (b) SPM concentration, and (c) SPM flux against alongshore wind stress estimated from buoy 45006 data. SPM concentration and SPM flux are estimates at 0.4 mab. Positive alongshore wind stress is directed to the northeast and is downwelling favorable.

[58] This tendency for bottom stress and SPM concentration to be greater for storm-driven downwelling, as opposed to upwelling, events would account for the relatively large mean offshore eddy fluxes of the late season deployments of 1999 and 2000 (Table 4).

5. Summary and Discussion

[59] Our data clearly reveal a distinct seasonal pattern of the near-bottom currents over the Keweenaw slope, marked by persistently weak currents during summer and frequent episodes of strong northeastward flows during autumn and winter. As noted earlier, this pattern appears to be partly due to a seasonal change in the wind field over central Lake Superior. During both study years, northeastward winds tended to be more frequent and stronger in the autumn and winter than in the spring and summer. Another factor that may contribute to the seasonal change in the near-bottom slope environment is a seasonal expansion of the non-wind-driven component of the Keweenaw Current. There is currently no published data that clearly reveals such an expansion, although recent modeling results indicate that the offshore extent of the Keweenaw Current tends to increase throughout the summer and autumn (C. Chen, personal communication).

[60] Many of findings of our study relate to properties that must be considered when modeling bottom stress and sediment resuspension within Lake Superior. One such property is the strength of near-bottom currents due to surface waves. During vigorous storms, wave-current interaction is seen to dominate bottom stress generation over the outer shelf and appreciably influence bottom stresses over much of the Keweenaw slope. Also of potential importance is the spatial variation of physical bottom roughness. Our results indicate that bottom roughness over the shelf may be significantly higher (by roughly a factor of 5) than bottom roughness over the slope (Table 2). What may be particularly challenging to account for in numerical models is the temporal variation in threshold resuspension stress indicated by the analyses of autumn and winter data.

[61] Our measurement have also revealed that high-frequency motions in the internal wave band are of fundamental importance in generating bottom stress at locations where the seasonal thermocline intersects the bottom. Over the Keweenaw slope, the impact of internal waves on bottom stress generation can appreciably exceed that of orbital velocities due to surface waves. This is clearly illustrated by the stresses computed from data acquired at 60 m during the autumn 1999 deployment. For events of high bottom stress, the elimination of high-frequency motions from stress computation using these data reduce the resultant stress estimate by a factor of two more than estimated stress is reduced through the elimination of orbital wave velocities due to surface waves. Clearly, the enhancement of bottom stress by internal wave currents may significantly impact the mobilization of slope sediments.

[62] The net transport of material resuspended over the slope appears to be controlled, in part, by the coincidence in the directions of downwelling favorable alongshore wind and the non-wind-driven component of the Keweenaw Current. This coincidence results in higher bottom stresses during downwelling, as opposed to upwelling, circulation, and is shown to be an important factor contributing to the net offshore sediment transport seen during autumn and winter. Because buoyancy-driven coastal currents typically flow in the direction of the downwelling favorable alongshore wind, this may be a phenomenon important to the sedimentary regime of many coastal regions.

[63] **Acknowledgments.** We are especially grateful to Noel Urban and Jaebong Jeong for supplying the grain size data used to generate Figure 3 and to Steve Manganini and Julianne Palmieri for their analyses of the in situ suspended particulate samples. We much appreciate the comments and suggestions offered by Larry Sanford and Charles Kerfoot throughout the course of this study and in the preparation of this manuscript. Our manuscript was greatly improved because of the comments and suggestions offered by Glen Gawarkiewicz and two anonymous reviewers. Our gratitude goes to all of those who took part in the tripod assembly and deployment operations. These include Angela Cates, Matthew Churchill, Chris Lumping, James Musielewicz, Brian Rajdl, Ralph Rincones, Bridget Thompson. Finally, our thanks to the crew of the R/V *Blue Heron*: Captain Mike King, Richard Laubly, Monica Scheflo, Issac Larsen, Rosanne Scott, and John Simenson. The work described was part of the Keweenaw Interdisciplinary Transport Experiment in Superior funded by the National Science Foundation through grants 9712889 to J. Churchill and A. Williams and 9712871 to E. Ralph. WHOI contribution 11057.

References

Bendat, J. S., and A. G. Piersol (1971), *Random Data: Analysis Measurement Procedures*, Wiley-Interscience, Hoboken, N. J.

Bogucki, D., T. Dickey, and L. G. Redekopp (1997), Sediment resuspension and mixing by resonantly generated internal solitary waves, *J. Phys. Oceanogr.*, *27*, 1181–1196.

Butman, B. (1987), Physical processes causing surficial sediment movement, in *Georges Bank*, edited by J. H. Ryther and J. W. Farrington, pp 147–162, MIT Press, Cambridge, Mass.

Cacchione, D. A., and D. E. Drake (1986), Nepheloid layers and internal waves over continental shelves and slopes, *Geo Mar. Lett.*, *6*, 147–152.

Cacchione, D. A., and J. B. Southard (1974), Incipient sediment movement by shoaling internal gravity waves, *J. Geophys. Res.*, *79*, 2237–2242.

Cacchoine, D. A., W. D. Grant, D. E. Drake, and S. M. Glenn (1987), Storm-dominated bottom boundary layer dynamics on the northern California continental shelf: Measurements and predictions, *J. Geophys. Res.*, *92*, 1817–1827.

Chen, C., J. Zhu, E. A. Ralph, S. A. Green, J. W. Budd, and F. Y. Zhang (2001), Prognostic modeling studies of the Keweenaw Current in Lake Superior. Part I: Formation and evolution, *J. Phys. Oceanogr.*, *31*, 379–395.

Chen, C., Q. Xu, E. Ralph, J. W. Budd, and H. Lin (2004), Response of Lake Superior to mesoscale wind forcing: A comparison between currents driven by QickSCAT and buoy winds, *J. Geophys. Res.*, doi:10.1029/2002JC001692, in press.

Churchill, J. H., C. D. Wirick, C. N. Flagg, and L. J. Pietrafesa (1994), Sediment resuspension over the continental shelf east of the Delmarva Peninsula, *Deep Sea Res., Part II*, *41*, 341–363.

Csanady, G. T., J. H. Churchill, and B. Butman (1988), Near-bottom currents over the continental slope in the Mid-Atlantic Bight, *Cont. Shelf Res.*, *8*, 653–671.

Flagg, C. N. (1988), Internal and mixing along the New England shelf-slope front, *Cont. Shelf Res.*, *8*, 737–756.

Grant, W. D., and O. S. Madsen (1979), Combined wave and current interaction with a rough bottom, *J. Geophys. Res.*, *84*, 1797–1808.

Grant, W. D., and O. S. Madsen (1982), Movable bed roughness in unsteady oscillatory flow, *J. Geophys. Res.*, *87*, 469–481.

Green, T., and R. E. Terrell (1978), The surface temperature structure associated with the Keweenaw Current in Lake Superior, *J. Geophys. Res.*, *83*, 419–426.

Harris, C. K., and P. L. Wiberg (2001), A two-dimensional, time-dependent model of suspended sediment transport and bed reworking for continental shelves, *Comput. Geosci.*, *27*, 675–690.

Hawley, N. (2000), Sediment resuspension near the Keweenaw Peninsula, Lake Superior during the fall and winter 1990–1991, *J. Great Lakes Res.*, *26*, 495–505.

Hawley, N., and C. H. Lee (1999), Sediment resuspension and transport in Lake Michigan during the unstratified period, *Sedimentology*, *46*, 791–806.

Hawley, N., and B. M. Lesht (1995), Does resuspension maintain the benthic nepheloid layer in sourtheastern Lake Michigan?, *J. Sediment Res., Sect. A*, *65*, 69–76.

Hawley, N., X. Wang, B. Brownawell, and R. D. Flood (1996), Sediment resuspension in Lake Ontario during the unstratified period, 1992–1993, *J. Great Lakes Res.*, *22*, 707–721.

Kang, S. W., Y. P. Sheng, and W. Lick (1982), Wave action and bottom shear stresses in Lake Erie, *J. Great Lakes Res.*, *8*, 482–494.

Lee, C. H., and N. Hawley (1998), The response of suspended particulate material to upwelling and downwelling events in southern Lake Michigan, *J. Sediment Res.*, *68*, 819–831.

Li, M. Z., and C. L. Amos (2001), SEDTRANS96: The upgraded and better calibrated sediment-transport model for continental shelves, *Comput. Geosci.*, *27*, 619–645.

Liu, P. C., D. J. Schwab, and J. R. Bennett (1984), Comparison of a two-dimensional wave prediction model with synoptic measurements in Lake Michigan, *J. Phys. Oceanogr.*, *14*, 1514–1518.

Longuet-Higgins, M. S. (1952), On the statistical distribution of the heights of sea waves, *J. Mar. Res.*, *11*, 245–266.

Lou, J., D. J. Schwab, D. Beletsky, and N. Hawley (2000), A model of sediment resuspension and transport dynamics in southern Lake Michigan, *J. Geophys. Res.*, *105*, 6591–6610.

Lyne, V. D., B. Butman, and W. D. Grant (1990a), Sediment movement along the U. S. east coast continental shelf-II. Modeling suspended sediment concentration and transport rate during storms, *Cont. Shelf Res.*, *10*, 429–461.

Lyne, V. D., B. Butman, and W. D. Grant (1990b), Sediment movement along the U.S. continental shelf-I. Estimates of bottom stress using the Grant-Madsen-Glenn model and near-bottom wave and current measurements, *Cont. Shelf Res.*, *10*, 397–428.

Niebauer, H. J., T. Green, and R. A. Ragotzkie (1977), Coastal upwelling/downwelling cycles in southern Lake Superior, *J. Phys. Oceanogr.*, *7*, 918–927.

Nikuradse, J. (1933), Stromungsgesetz in rauhren rohren, vdi forschungsheft 361, *NACA Tech. Memo. 1292*, Natl. Advis. Comm. for Aeronaut., Washington, D. C.

Schwab, D. J., D. Beletsky, and J. Lou (2000), The 1998 coastal turbidity plume in Lake Michigan, *Estuarine Coastal Shelf Sci.*, *50*, 49–58.

Sherwood, C. R., B. Butman, D. A. Cacchione, D. E. Drake, T. F. Gross, R. W. Sternberg, P. L. Wiberg, and A. J. Williams III (1994), Sediment transport events on the northern California continental shelf during the 1990–1991 STRESS experiment, *Cont. Shelf Res.*, *14*, 1063–1099.

Traykovski, P., A. E. Hay, J. D. Irish, and J. F. Lynch (1999), Geometry, migration, and evolution of wave orbital ripples at LEO-15, *J. Geophys. Res.*, *104*, 1505–1524.

Wiberg, P. L., and D. M. Rubin (1989), Bed roughness produced by saltating sediment, *J. Geophys. Res.*, *94*, 5011–5016.

Wiberg, P. L., D. E. Drake, and D. A. Cacchione (1994), Sediment resuspension and bed armoring during high bottom stress events on the northern California inner continental shelf: Measurements and predictions, *Cont. Shelf Res.*, *14*, 1191–2119.

Williams, A. J., III, J. S. Tochko, R. L. Koehler, W. D. Grant, T. F. Gross, and C. R. V. Dunn (1987), Measurement of turbulence in the oceanic bottom boundary layer with an acoustic current meter array, *J. Atmos. Oceanic Technol.*, *4*, 312–327.

Xu, J. P., and L. D. Wright (1995), Tests of bed roughness models using field data from the Middle Atlantic Bight, *Cont. Shelf Res.*, *15*, 1409–1434.

Yeske, L. A., and T. Green III (1975), Short-period variations in a Great Lakes coastal current by aerial photogrammetry, *J. Phys. Oceanogr.*, *5*, 125–135.

Zhu, J., C. Chen, E. A. Ralph, S. A. Green, J. W. Budd, and F. Y. Zhang (2001), Prognostic modeling studies of the Keweenaw Current in Lake Superior. Part II: Simulation, *J. Phys. Oceanogr.*, *31*, 396–410.

J. H. Churchill and A. J. Williams, Woods Hole Oceanographic Institution, Woods Hole, MA 02543, USA. (jchurchill@whoi.edu)

E. A. Ralph, Large Lakes Observatory, University of Minnesota at Duluth, Duluth, MN 55812, USA.